

Forecasts of ENSO evolution using spatial-temporal projection model

Xiao Pan¹, Zhiwei Zhu^{1*}, Tim Li^{1,2}

1, Key Laboratory of Meteorological Disaster, Ministry of Education (KLME)/Joint International Research Laboratory of Climate and Environment Change (ILCEC)/Collaborative Innovation Center on Forecast and Evaluation of Meteorological Disasters (CIC-FEMD), Nanjing University of Information Science and Technology, Nanjing, China

2, International Pacific Research Center and Department of Atmospheric Sciences, University of Hawaii at Manoa, Honolulu, Hawaii

Corresponding author: Zhiwei Zhu, Nanjing University of Information Science and Technology, Ningliu Road 219, Meteorology Bldg. Jiangsu 210044, China.

E-mail: zwz@nuist.edu.cn

This article has been accepted for publication and undergone full peer review but has not been through the copyediting, typesetting, pagination and proofreading process which may lead to differences between this version and the Version of Record. Please cite this article as doi: 10.1002/joc.6581

Abstract

ENSO prediction is one of the most debated and challenging tasks, whilst its real-time operational prediction skill still has room for improvement. In this study, spatial-temporal projection model is applied to predict Niño3.4 index at lead time of one to six months. By regressing variable fields onto Niño3.4 index month by month, physical-based predictability sources, i.e., the mixed-layer oceanic temperature, sea surface temperature, thermocline depth, and accumulated westerly-wind-events index over the specific regions are detected as the predictors. Based on the temporal evolution of coupled modes of predictors and Niño3.4 index, the Niño3.4 index from JAS (July, August and September) to DJF (December, January and February) can be predicted once a year.

The model could nicely reproduce the evolution of Niño3.4 index from JAS to DJF. It also achieved high prediction skills for the year-to-year DJF Niño3.4 index, with a root-mean-square error of 0.46 in the training period (1950–2000) and 0.52 in the independent-forecast period (2001–2016). Further investigation shows that the forecast is more reliable when the forecasted ENSO amplitude is much larger.

Keywords

ENSO prediction; ENSO evolution; spatial-temporal projection model

1. Introduction

Given that El Niño–Southern Oscillation (ENSO) has enormous impacts on global climate/weather through inducing various atmospheric teleconnections, such as Pacific North America pattern (Wallace and Gutzler, 1981; Horel and Wallace, 1981; Hoskins and Karoly, 1981), Pacific East Asia teleconnection (Wang et al., 2000; Wang et al., 2017), Pacific Japan pattern (Molinari and Vollaro, 2017; Srinivas et al., 2018), Asia North America pattern (Zhu and Li, 2016; 2018a) and North Atlantic Oscillation (Chen et al., 2015; Cai et al., 2018; Park and Li, 2018), how to accurately predict ENSO has long been a hot topic in the climatology/hydrology community. Although numerous theories have been proposed to explain ENSO dynamics (Cane and Zebiak, 1985; Suarez, 1988; Battisti and Hirst, 1989; Neelin et al., 1990; Jin, 1997; Li, 1997; Weisberg and Wang, 1997; Picaut et al., 1997), the ENSO diversity in terms of the spatial pattern (Yu and Kim, 2011; Dommenges et al., 2013), the evolution (Kessler, 2002; Larkin and Harrison, 2002; McPhaden and Zhang, 2009; Kim et al., 2011; Chen et al., 2016), and the intensity (Burgers and Stephenson, 1999; Jin et al., 2003; An and Jin, 2004; Su et al., 2010) bring a big challenge to the success of the operational ENSO forecasting.

Both dynamical models and statistical models are avenues to unravel the dilemma of ENSO prediction. By assimilating subsurface information into oceanic general circulation model, the coupled general circulation models, such as Scale Interaction Experiment—Frontier Research Center for Global Change coupled model (Luo et al., 2005; 2007) and the European Centre for Medium-Range Weather Forecasts system 5 (Johnson et al., 2019), have improved the forecast skills of Niño3.4 index greatly. Besides, the statistical methods, such as linearized intermediate coupled ENSO model (Morss and Battisti, 2004), nonlinear dimensionality reduction method (Lima et al., 2009), convolutional neural network method (CNN, Ham et al., 2019) and machine learning algorithms (Pal et al., 2020), also use subsurface signals as predictors to predict ENSO events 17 months in advance.

Geert et al. (2005) pointed out that the dynamical models are better at predicting the onset of ENSO while the statistical models show encouraging skills at predicting the evolution of ENSO. Barnston et al. (2012) presented that the ensemble of the dynamical models slightly outperforms that of statistical models for the better performance during spring predictability barrier. Though

the performance of dynamical models is often comparable or even better than the statistical models, the statistical models are still the complementary tools. For instance, most of the dynamical models failed to predict the 2015/16 El Niño (see Fig. S1 of the supplemental material). Moreover, while the statistical model is simple and cheap, its predictive skill is often comparable to that of complicated and expensive dynamical models.

In recent years, different kinds of statistical models, the spatial-temporal projection models (STPM), were proposed for extended-range forecasts of the atmospheric low-frequency evolution (i.e., the intraseasonal oscillation), with several models having been operationally applied with encouraging skills (Zhu et al., 2015; Zhu and Li, 2017; 2018b). By obtaining significant predictor-predictand coupled modes through cross-validation during the training period, the predictand can be predicted by the predictand modes and the corresponding time series, which is reconstructed by projecting the predictors onto the predictor modes (see section 2.2 for details). Since that STPM have the specialty in capturing the evolution of the climate variability, can the newly developed STPM be applied in predicting ENSO? It may be a good attempt to construct a STPM for predicting ENSO evolution based on reliable predictors.

Previous studies have identified numerous ENSO predictors, such as sea surface temperature (SST, Wang et al., 2012; Zhu et al., 2016), sea level height (Zhu, 2018), thermocline depth (Lima et al., 2009), and warm water volume (Monetti et al., 2002; McPhaden, 2003; Chen et al., 2017; Neske and McGregor, 2018) over the specific basins. Specifically, it has been known that models with the information of the ocean subsurface thermal condition could produce better skills at longer time lead in ENSO prediction (Lima et al., 2009). Besides, atmospheric signals, such as westerly wind bursts, are another key precursor (Tangang et al., 1997; Chen et al., 1997; Ineson et al., 2018) for ENSO development.

Thus, based on the existing knowledge on precursors of ENSO and the specialty of the STPM, in the present paper, we intend to construct STPM to predict ENSO evolution using multiple predictors. Both atmospheric (wind stress) and oceanic (SST and subsurface ocean data) variables, which are beneficial to obtain better predictive skills at longer lead time or favorable to well capture the extreme events, are employed as potential predictors to construct the STPM. The remainder of the paper is organized as follows. Section 2 describes the data and methods used in

the paper. Section 3 introduces the predictors, and section 4 presents the predicted results. Conclusion and discussion are given in the final section.

2. Data and methods

2.1 Data

Given that the vertical profile of mixed-layer temperature anomaly (MLTA) plays an important role in triggering ENSO episodes (McPhaden, 2003; Wang et al., 2004; Chen et al., 2016; Neske and McGregor, 2018), the present of the SST anomaly (SSTA) is essential to ENSO development (Monetti et al., 2002; McPhaden, 2003), the thermocline depth anomaly (D20CA) is important during ENSO formation (Su et al., 2010; Chen et al., 2017), and the accumulated westerly wind burst events index (AWI) could initiate the ENSO developing (Mcphaden, 1999; Chen et al., 2017; Ineson et al., 2018), these four predictability sources (i.e., MLTA, SSTA, D20CA, AWI) are selected in the present study.

The datasets to calculate these predictability sources include: (1) the monthly Extended Reconstructed SST analyses, version 5 (ERSST.v5), at a $2^\circ \times 2^\circ$ horizontal resolution (Huang et al., 2017); (2) the monthly mixed-layer ocean temperature analyses from Simple Ocean Data Assimilation, version 2.2.4 (SODAv2.2.4) (Carton et al., 2000), at a $0.5^\circ \times 0.5^\circ$ horizontal resolution and 40 vertical levels and the NCEP Global Ocean Data Assimilation System (GODAS) (Saha et al., 2006) at a 1° zonal resolution, $1/3^\circ$ meridional resolution, and 40 vertical levels with a 10-m resolution in the upper 105 m; (3) monthly thermocline depth (20°C isotherm depth) data from SODAv2.2.4 and GODAS; and (4) NCEP/NCAR reanalysis daily wind stress (Kalnay et al., 1996) data at a $1^\circ \times 1^\circ$ horizontal resolution. The daily zonal wind stress is used to calculate the AWI. Note that the thermocline depth may be a missing value in some years because the SST in the eastern Pacific may get lower than 20°C ; however, we have checked that missing values only account for less than 5% of the total time period, and the calculation based on the thermocline depth already excludes the missing values, so the calculation of thermocline depth are reliable.

All datasets cover the period 1950–2016, except for SODAv2.2.4, which covers 1950–2008, while GODAS covers 2009–2016. Because a long-term dataset is needed to construct the model in

a training period and to make a verification in an independent forecast period, we therefore combine the two datasets (SODAv2.2.4 and GODAS) together. Nevertheless, the predictability sources obtained from the two datasets during the overlapping period of 1980–2008 are quite consistent, suggesting that it is reasonable to combine these two independent datasets as a whole. In addition, the datasets (except SODAv2.2.4) are real-time updated, which could facilitate a real-time forecast. The monthly anomalies are calculated by subtracting their climatological mean during 1981–2010. All the datasets are first interpolated into a $2^\circ \times 2^\circ$ horizontal resolution via bilinear interpolation.

The Niño3.4 index is defined by the SSTA averaged over (5°S – 5°N , 170° – 120°W) with a three-month running-mean.

2.2 Spatial-temporal projection model

The running of the spatial-temporal projection model (STPM) follows Zhu et al. (2015), which comprised the singular value decomposition (SVD; Bretherton et al., 1992), cross-validation, and independent-forecast processes (Fig. 1).

The first step in the STPM is to perform SVD between the standardized predictand (Y) and each standardized predictor field (X) in the training period (1950–2000, 51 years in total). This extracts the coupled temporally evolving modes of the predictors and predictand. In SVD (equations 1 and 2), the time series of predictors (u_k) are highly correlated to that of the predictand (v_k).

$$X(t, i_1 \times j_1 \times n_1) \approx \sum_{k=1}^K U_k(i_1 \times j_1 \times n_1) u_k(t) \quad (1)$$

$$Y(t, i_2 \times j_2 \times n_2) \approx \sum_{k=1}^K V_k(i_2 \times j_2 \times n_2) v_k(t) \quad (2)$$

where U_k and V_k are the k th modes coupled of the predictor and predictand; i_1 (j_1) and i_2 (j_2) are the zonal (meridional) grids for the predictor and predictand fields; t represents the temporal grids; n_1 (n_2) denotes n_1 (n_2) months lead (lag) to the time t in the training period.

The cross-validation is carried out after the SVD during the training period. The procedure is as follows: Firstly, exclude one year's data and perform SVD using the remaining 50 years' data during the training period. Then, project the excluded one-year predictor and predictand onto the SVD modes based on the 50 years data to get the one year of six pair of time series. Next, repeat

the above two steps 50 times to obtain 51 years of six pairs of time series of the coupled predictors-predictand SVD modes. Finally, calculate the correlation coefficients between the six pairs of time series and obtain the corresponding significant SVD modes that exceed the 99% confidence level. The total number of valid SVD modes is M .

The independent forecast is produced after cross-validation has been performed. The predictors in the forecast period (2001-2016) are projected on the valid SVD spatial modes (U_m) derived from the cross-validation part to obtain each predictor's time series (u_m) (see equation 3). Then, the predictand's time series (v_m) is substituted with the predictor's (u_m) because of the high correlation between them, and then by summing the valid spatial modes of the predictand (V_m) and its corresponding time series (u_m), the predictand (Y_p) in the forecast period is obtained (see equation 4).

$$u_m(t_p) = \sum_{s=1}^{i_1 \times j_1 \times n_1} X(t_p, i_1 \times j_1 \times n_1) \times U_m(i_1 \times j_1 \times n_1) \quad (3)$$

$$Y_p(t_p, i_2 \times j_2 \times n_2) \approx \sum_{m=1}^M V_m(i_2 \times j_2 \times n_2) u_m(t_p) \quad (4)$$

where t_p is the independent forecast period; m and M indicate the m th and total number of SVD modes exceeding the significance level of 99% during cross-validation.

To modify the amplitude of Y_p , the ratio between the standard deviation of the observed and reconstructed predictand fields by useful modes during 1950-2000 is used to multiply Y_p . As equation 5 shows, Y_p^* is the final forecasted predictand.

$$Y_p^*(t_p, i_2 \times j_2 \times n_2) = Y_p(t_p, i_2 \times j_2 \times n_2) \cdot ratio(i_2 \times j_2 \times n_2) \quad (5)$$

The predictors are four variables (MLTA, SSTA, D20CA and AWI) from Feb.(0) to Jul.(0) with a one-month interval, and the predictand is Niño3.4 index from JAS(0) to DJF(+1) with a one-month interval during each year (the basis for selecting the predictors is shown in detail in the next section). Therefore, in each year, the predictor and predictand both have six time points. Here, the notation '(0)' and '(+1)' means the current year and the following year, respectively. In addition, to reduce the systematic bias on the mean state of SST and to retain the SST tendency, the final predicted Niño3.4 index Y_{valid}^* is modified according to the following equation:

$$Y_{valid}^* = Y_p^* - (Y_{JAS}^* - Obs_{Jul}) \quad (6)$$

where Y_p^* is the predicted Niño3.4 index in the independent forecast period, Y_{JAS}^* is the predicted

JAS(0) Niño3.4 index, Obs_{Jul} is the observed Jul.(0) Niño3.4 index.

To test the fidelity of the STPM, we also select 1950–1990 as the training period and 1991–2016 as the independent-forecast period to rerun the STPM, the forecast skills are quite consistent (see Figs. S2-S6 in the supplementary material).

3. Selection of predictors

As mentioned in section 2, four predictability sources (i.e., MLTA, SSTA, D20CA, AWI) are selected. By regressing predictability sources from Oct.(–1) to Jul.(0) onto JAS(0) (SON(0), NDJ(0)) Niño3.4 index month by month, we select the boxes that contain the most useful time-varying information of each predictor field. The selected predictors are MLTA (5–105 m, 120°E–80°W, and averaged over 5°S–5°N), SSTA (5°S–5°N, 160°E–80°W), D20CA (5°S–5°N, 160°–100°W), and AWI (accumulated based on 5°S–5°N, 120°E–180°). While the details of the four predictors are provided in Table 1, the reasons for the selection of these predictors are as follows.

The maximum positive (negative) anomalous temperature in the subsurface contributes to positive (negative) temperature advection through mean upwelling by thermocline feedback ($-\bar{w} \frac{\partial T'}{\partial z}$), then leading to SST warming in the eastern Pacific (i.e., the evolution of MLTA can be highly connected with the SSTA in the eastern and central Pacific). Figure 2 shows MLTA regressed on Niño3.4 index averaged in two-month intervals. For example, in the top panel of Fig. 2, Oct.(–1) represents the average of Oct.(–1) and Nov.(–1) MLTA regressed onto JAS(0) Niño3.4 index. MLTA is significantly positive over the western Pacific in Oct.(–1), whereas in the central and eastern Pacific (CEP) this is the case during Feb.(0) to Jul.(0), meaning the key pattern associated with ENSO evolution appears within (5–105 m, 120°E–80°W). Therefore, the MLTA (5–105 m, 120°E–80°W, and averaged over 5°S–5°N) is selected as the predictor.

Figure 3 shows the SSTA pattern regressed on Niño3.4 index averaged in two-month intervals. A positive SSTA is significant in the CEP during Feb.(0) to Jul.(0). The CEP SSTA pattern is essential to the Niño3.4 index forecast because of the SST persistence. Therefore, we select (5°S–5°N, 160°E–80°W) as another predictor.

The thermocline depth anomaly has a relationship with ocean currents and plays an important role in ENSO evolution. The relationship between the thermocline depth anomaly and ocean currents is as follows:

$$u_g' = -\frac{g'}{\beta} \frac{\partial^2 h'}{\partial y^2}, \quad (7)$$

where u_g' is the anomalous geostrophic current, $g' = 0.026 \text{ m s}^{-1}$ is the reduced gravity, β is the planetary vorticity, and h' is the thermocline depth anomaly. This means that a positive (negative) thermocline depth anomaly along the equator will lead to positive (negative) geostrophic currents, while the geostrophic currents anomaly determines the ocean zonal current anomaly (Su et al., 2010). An anomalous positive (negative) zonal current contributes to warm (cold) temperature advection by zonal advection feedback ($-u' \frac{\partial \bar{T}}{\partial x}$). Figure 4 shows the D20CA pattern regressed onto Niño3.4 index averaged every two months. D20CA is moderately significant in Dec.(-1) and more significant from Feb.(0) to Jul.(0). It is observed that the varying information of D20CA is confined to the region of the (5°S–5°N, 160°–100°W), therefore, the D20CA (5°S–5°N, 160°–100°W) is selected as the third predictor.

Besides, the AWI is selected as the final predictor because the onset of El Niño can be determined by the westerly wind burst events (WWE) in the western Pacific. The pulses of WWE-Taux' (see Table 1 for the definition) match well with the flaring up of h' over the CEP. WWE forcing may play an essential role in the sudden emergence and continuous intensification of positive h' over the CEP, thus contributing to ENSO formation (Chen et al. 2017).

After selecting the four predictors of MLTA, SSTA, D20CA and AWI, The STPM for forecasting ENSO evolution is conducted, and the forecast skills are evaluated in the following section.

4. Prediction skills

4.1 ENSO evolution in a year

The independent-forecast period covers 2001–2016, while the predicted Niño3.4 index is compared with the observation. RMSE is used to measure the prediction skills.

Fig. 5 shows the Niño3.4 index evolution predicted by MLTA and the observation. During the

independent period (2001–2016), especially for the 2015 super El Niño, the predicted Niño3.4 index matches the observed SSTA tendency well. Twelve (2001, 2002, 2003, 2004, 2008, 2010, 2011, 2012, 2013, 2014, 2015, 2016) out of sixteen years have the RMSE less than 0.4, and the best skill appears in 2014 with a RMSE of 0.08. When the predicted and the observed DJF Niño3.4 index are both more (less) than 0.5°C (-0.5°C), a correct forecast of ENSO event is defined. Therefore, 11 years (2001, 2002, 2003, 2004, 2007, 2008, 2009, 2010, 2011, 2014, 2015) are correctly forecasted using the MLTA as the predictor. The accuracy of the forecast accounts for 69% of the total sixteen cases.

Fig. 6 shows the observed and the SSTA predicted Niño3.4 index evolution. RMSE of eight (2001, 2002, 2003, 2004, 2008, 2013, 2014, 2015) years are less than 0.4, and the best two years are 2003 and 2014. The prediction by D20CA as shown in Fig. 7 are also reasonable. Eleven (2001, 2002, 2003, 2004, 2008, 2010, 2011, 2012, 2013, 2014, 2016) out of sixteen years have the RMSE less than 0.4, and the best one is 2001.

Figure 8 shows observed Niño3.4 index and Niño3.4 index predicted by AWI. There are eight (2001, 2003, 2004, 2009, 2010, 2013, 2014, 2016) years with RMSE less than 0.4. It correctly forecast the ENSO events in 2003, 2004, 2007, 2009, 2010, 2011, 2014, 2015 and 2016, accounting for 56%.

Among the above forecasts by the four predictors, the RMSE of 2001, 2003, 2004, 2013 and 2014 is always smaller than 0.4, and the SSTA tendencies in 2014 and 2015 match well with the observations. The overall ENSO developing characteristics are captured well by STPM.

4.2 Year-to-year DJF Niño3.4 index

Because Niño3.4 index in DJF reflects the mature phase of ENSO, in this section, we evaluate the forecast skill of STPM in forecasting DJF Niño3.4 index at lead time of 6 months. Figure 9 shows the year-to-year predicted and observed DJF Niño3.4 index. The hindcast is conducted during 1950-2000 and the independent-forecast period is 2001-2016. Among the four predictors, D20CA has the minimum RMSE and performs better than the other three predictors. However, because the best predictor for any particular year is different, an ensemble-mean strategy of the forecasts from four different predictors (with equal weights) is employed. The

RMSE of the ensemble-forecast DJF Niño3.4 index is 0.46 in the training period and 0.52 in the independent forecast period at lead of 6 months. The forecast skill is higher than both the persistent forecast (Fig. 9) and BCC_CSM forecast (Fig. S1b).

According to the amplitude of predicted DJF Niño3.4 index rather than observation, the forecasted ENSO can be divided into three categories, the predicted normal events (amplitude less than 0.5°C), the predicted weak ENSO events (amplitude more than 0.5°C and less than 1°C) and the predicted strong ENSO events (amplitude more than 1°C). The correlation coefficient between the observed (y-axis) and the predicted (x-axis) Niño3.4 index in each category is calculated (Fig. 10). When forecast indicates a coming weak ENSO event, the forecast is often more accurate (with a correlation coefficient of 0.66) than that of normal events (with a correlation coefficient of 0.51). Besides, the forecasted strong ENSO events are more reliable than the weak ones (0.95 vs 0.66), suggesting that the forecast reliability is increasing with the forecast ENSO intensity.

The persistence Niño3.4 prediction is also shown in Fig. 10. It is clear that for both La Niña and El Niño, the ensemble-mean model forecast is always closer to the observation than that of the persistent forecast. The persistent forecast underestimates the amplitude of the ENSO while the STPM forecasting can reproduce more realistic Niño3.4 index.

5. Conclusion and discussion

5.1 Conclusion

In this paper, based on the spatial temporal projection method proposed by Zhu et al. (2015), we conduct an STPM to forecast Niño3.4 index at lead time of one to six months. By regressing physical-based predictability sources onto Niño3.4 index month by month, we select four predictors, the MLTA (5°S – 105°W , 120°E – 80°W , and averaged over 5°S – 5°N), the SSTA (5°S – 5°N , 160°E – 80°W), the D20CA (5°S – 5°N , 160° – 100°W), and the AWI (accumulated based on 5°S – 5°N , 120°E – 180°) from Feb. to Jul. to construct the STPM to forecast the Niño3.4 index from JAS to DJF. It is shown that STPM based on four predictors can capture the ENSO events well in 2014 and 2015; and among the four predictors, D20CA shows the best skill of RMSE. Because each year has the different best predictor, an ensemble strategy is employed. The RMSE of ensemble-mean forecast Niño3.4 index at lead of six months reaches 0.46 in the training period

and 0.52 in the independent forecast period. The prediction skill of the ensemble-mean forecast is higher than persistent forecast (Fig. 9) and BCC_CSM forecast (Fig.S1b).

However, for some years, such as 2005, 2006 and 2012, Niño3.4 index is not well predicted. This might be because of the interaction between the Pacific and other ocean basins, or stochastic disturbance effects from the atmosphere. Although the individual forecasts have inevitable errors, the RMSE ranges from 0.20 to 0.52 with lead time from one to six months (see Table 2), suggesting that the pure statistical STPM can capture the ENSO evolution quite well. The STPM can well reproduce the year-to-year variability of DJF Niño3.4 index with a RMSE of 0.52 at lead time of six months. Further investigation shows that the forecast reliability is increasing with the forecast ENSO amplitude.

5.2 Discussion

Note that the ensemble of the individual STPM at lead of six months is employed and the prediction skill is relatively high. However, building one model that based on multiple predictors could be an alternative option, and the forecast skill may be also encouraging. Currently, forecasts are faced with dilemma (Lerch et al., 2017). On the one hand, public typically focus on the predictive performances in extreme events for the quality of forecasts. On the other hand, even the most skillful models could fail when the signal-to-noise ratio is too low (Fig. S1 in the supplementary material). Our work shows the predicted strong ENSO events are more reliable than other events, which encourages us to trust the forecast of the extreme events (Jin et al. 2008).

Note that although the RMSE skill of STPM is high in forecasting ENSO evolution, the relationship between the predictors and predictand may still undergo secular changes. To avoid the effect from the selection the forecasting period and verify the model fidelity, we also choose the 1950-1990 as the training period and the 1991-2016 as the independent forecast period to rerun the model, and the forecast skills are quite consistent (see Figs. S2-S6 in the supplementary material). The forecast skills of STPM with cross-validated modes may not dramatically drop in the next decades, and the discipline in the training period should be universal for the near-future independent forecast period. However, the behavior of ENSO is still uncertain under the context of global climate change (Chen et al., 2015), resulting in the shortcoming and limitation of STPM.

In the present study, predictors are selected only from Pacific Ocean, however, signals from the Atlantic or Indian Ocean basins are also important in ENSO formation and evolution. The STPM could be further refined when considering the pantropical climate interaction of inter-basins (Cai et al., 2019).

Acknowledgements

This work was supported by the National Key R&D Program of China (Grant No. 2018YFC1505803), the National Natural Science Foundation of China (Grant Nos. 41605035 and 41805048) and the Young Elite Scientists Sponsorship Program by CAST (2018QNRC001).

References

- An SI, Jin FF. 2004. Nonlinearity and Asymmetry of ENSO. *J. Clim.* **17**(14): 2851-2865.
- Andréa ST, Gupta AS, Jourdain NC, et al. 2014. Cold tongue and warm pool ENSO Events in CMIP5: Mean state and future projections. *J. Clim.* **27**(8).
- Barnston AG, Tippett MK, L'Heureux ML, et al. 2012. Skill of real-time seasonal ENSO model predictions during 2002–11: Is our capability increasing? *Bull. Amer. Meteor. Soc.* **93**: 631–651.
- Battisti DS, Hirst AC. 1989. Interannual variability in a tropical atmosphere-ocean model: Influence of the basic state, ocean geometry and nonlinearity. *J. Atmos. Sci.* **46**(12): 1687-1712.
- Bjerknes J. 1968. Atmospheric teleconnections from the equatorial Pacific. *Mon. Weather Rev.* **97**: 163-172.
- Bretherton CS, Smith C, Wallace JM. 1992. An intercomparison of methods for finding coupled patterns in climate data. *J. Clim.* **5**: 541–560.
- Burgers G, Stephenson DB. 1999. The “normality” of El Niño. *Geophys. Res. Lett.* **26**(8): 1027–1030.
- Cai WJ, Wu LX, Lengaigne M, et al. 2019. Pantropical climate interactions. *Sci.* **363**(6430).
- Carton JA, Chepurin G, Cao X, et al. 2000. A Simple Ocean Data Assimilation Analysis of the Global Upper Ocean 1950-95. Part I: Methodology. *J. Phys. Oceanogr.* **30**(2): 294-309.
- Chen L, Li T, Yu Y. 2015. Causes of Strengthening and Weakening of ENSO Amplitude under Global Warming in Four CMIP5 Models. *J. Clim.* **28**(8): 3250-3274.
- Chen L, Li T, Wang B, Wang L. 2017. Formation Mechanism for 2015/16 Super El Niño. *Sci. Rep.* **7**: 2975.
- Chen D, Zebiak SE, Cane MA. 1997. Initialization and predictability of a coupled ENSO forecast model. *Mon. Weather Rev.* **125**: 773-788.
- Chen M, Li T, Shen X, et al. 2016. Relative Roles of Dynamic and Thermodynamic Processes in Causing Evolution Asymmetry between El Niño and La Niña. *J. Clim.* **29**(6): 2201-2220.
- Chen S, Wu R, Chen W. 2015. The changing relationship between interannual variations of the

- North Atlantic oscillation and Northern Tropical Atlantic SST. *J. Clim.* **28**: 485 – 504.
- Dommenget D, Bayr T, Frauen C. 2013. Analysis of the non-linearity in the pattern and time evolution of El Niño southern oscillation. *Clim. Dyn.* **40**(11-12): 2825-2847.
- Ewel DKC. 2001. Effect of the 1997-1998 ENSO-related drought on hydrology and salinity in a micronesia wetland complex. *Estuaries.* **24**(3): 347-356.
- Graham NE, Barnett TP, Latif M. 1992. Considerations of the predictability of ENSO with a low-order coupled model. *TOGA Notes.* **7**: 11-15.
- Geert JVO, Balmaseda MA, Ferranti L, et al. 2005. Did the ECMWF Seasonal Forecast Model Outperform Statistical ENSO Forecast Models over the Last 15 Years? *J. Clim.* **18**(16): 3240-3249.
- Ham Y, Kim J, Luo J. 2019. Deep learning for multi-year ENSO forecasts. *Nature.* **573**: 568–572.
- Hoerling MP, Kumar A, Zhong M. 1996. El Niño, La Niña, and the Nonlinearity of Their Teleconnections. *J. Clim.* **10**(10): 1769-1786.
- Horel JD, Wallace JM. 1981. Planetary-Scale Atmospheric Phenomena Associated with the Southern Oscillation. *Mon. Weather Rev.* **109**: 813–829.
- Hsu PC, Li T, Lin YC, Lu MM, Lee JY. 2012. A spatial-temporal projection method for seasonal prediction of spring rainfall in northern Taiwan. *J. Meteorol. Soc. Jpn.* **90**: 179-190.
- Huang BY, Thorne PW, Banzon VF, Boyer T, Chepurin G, Lawrimore JH, Menne MJ, Smith TM, Vose RS, Zhang HM. 2017. NOAA Extended Reconstructed Sea Surface Temperature (ERSST), Version 5.
- Ineson S, Balmaseda MA, Davey MK, et al. 2018. Predicting El Niño in 2014 and 2015. *Sci. Rep.* **8**(1).
- Janicot S, Moron V, Fontaine B. 1996. Sahel droughts and Enso dynamics. *Geophys. Res. Lett.* **23**(5): 515-518.
- Jin EK, Coauthors. 2008. Current status of ENSO prediction skill in coupled ocean–atmosphere models. *Clim. Dyn.* **31**: 647-664.
- Jin FF. 1997. An equatorial ocean recharge paradigm for ENSO. Part I: Conceptual model. *J. Atmos. Sci.* **54**(7): 811-829.
- Jin FF, An SI, Timmermann A et al. 2003. Strong El Niño events and nonlinear dynamical heating. *Geophys. Res. Lett.* **30**(3): 20-1-20-4.
- Johnson SJ, Stockdale TN, Ferranti L, et al. 2019. SEAS5: the new ECMWF seasonal forecast system. *Geoscientific Model Development.* **12**(3): 1087-1117.
- Kalnay et al. 1996. The NCEP/NCAR 40-year reanalysis project. *Bull. Amer. Meteor. Soc.* **77**: 437-470.
- Kessler WS. 2002. Is ENSO a cycle or a series of events? *Geophys. Res. Lett.* **29**: 2125.
- Kim W, Yeh SW, Kim JH, Kug JS, and Kwon M. 2011. The unique 2009–2010 El Niño event: A fast phase transition of warm pool El Niño to La Niña. *Geophys. Res. Lett.* **38**: 15809.
- Kim HM, Webster PJ, Curry JA. 2012. Seasonal prediction skill of ECMWF System 4 and NCEP CFSv2 retrospective forecast for the Northern Hemisphere Winter. *Clim. Dyn.* **39**(12): 2957-2973.
- Kug JS, Jin FF, and An SI. 2009. Two types of El Niño events: Cold tongue El Niño and warm pool El Niño. *J. Clim.* **22**: 1499-1515.
- Larkin NK, and Harrison DE. 2002. ENSO warm (El Niño) and cold (La Niña) event life cycles: Ocean surface anomaly patterns, their symmetries, asymmetries, and implications. *J. Clim.* **15**:

- 1118–1140.
- Lerch S, Thorarinsdottir TL, Ravazzolo F, Gneiting T. 2017. Forecaster's Dilemma: Extreme Events and Forecast Evaluation. *Statist. Sci.* **32**: 106-127.
- Li T. 1997. Phase Transition of the El Niño-Southern Oscillation: A Stationary SST Mode. *J. Atmos. Sci.* **54**(54): 2872-2887.
- Lima CHR, Lall U, Jebara T, et al. 2009. Statistical Prediction of ENSO from Subsurface Sea Temperature Using a Nonlinear Dimensionality Reduction. *J. Clim.* **22**(17): 4501-4519.
- Luo JJ, Masson S, Behera SK, Yamagata T. 2007. Extended ENSO predictions using a fully coupled ocean-atmosphere model. *J. Clim.* **21**: 84-93.
- Luo JJ, Masson S, Roeckner E, Madec G, Yamagata T. 2005. Reducing climatology bias in an ocean-atmosphere CGCM with improved coupling physics. *J. Clim.* **18**: 2344-2360.
- Magorian PT. 1993. Prediction of Niño 3 Sea Surface Temperatures Using Linear Inverse Modeling. *J. Clim.* **6**(6): 1067-1076.
- McPhaden MJ. 1999. Genesis and evolution of the 1997–98 El Niño. *Sci.* **283**: 950–954.
- McPhaden MJ. 2003. Tropical Pacific Ocean heat content variations and ENSO persistence barriers. *Geophys. Res. Lett.* **30**(9): 1480.
- McPhaden MJ, and Zhang X. 2009. Asymmetry in zonal phase propagation of ENSO sea surface temperature anomalies. *Geophys. Res. Lett.* **36**: 13703.
- Molinari J, Vollaro D. 2017. Monsoon Gyres of the Northwest Pacific: Influences of ENSO, the MJO, and the Pacific-Japan Pattern. *J. Clim.* **30**(5):1765-1777.
- Monetti RA, Havlin S, Bunde A. 2002. Long term persistence in the sea surface temperature fluctuations. *Physica. A Statistical Mechanics & Its Applications.* **320**: 581-589.
- Morss RE, Battisti DS. 2004. Designing Efficient Observing Networks for ENSO Prediction. *J. Clim.* **17**(16): 3074-3089.
- Neelin JD, Battisti DS, Hirst AC et al. 1998. ENSO theory. *J. Geophys Res. Oceans.* **103**(C7): 14261-14290.
- Neske S, Mcgregor S. 2018. Understanding the Warm Water Volume Precursor of ENSO Events and its Interdecadal Variation. *Geophys. Res. Lett.* **45**(5).
- Ogotu GEO, Franssen WHP, Supit I, et al. 2017. Skill of ECMWF system-4 ensemble seasonal climate forecasts for East Africa. *Int. J. Climat.* **37**(5).
- Pal M, Maity R, Ratnam JV. 2020. Long-lead Prediction of ENSO Modoki Index using Machine Learning algorithms. *Sci. Rep.* **10**: 365.
- Park JH, Li T. 2018. Interdecadal modulation of El Niño–tropical North Atlantic teleconnection by the Atlantic multi-decadal oscillation. *Clim. Dyn.* **52**(9-10): 5345–5360.
- Picaut J, Masia F, Penhoat YD. 1997. An Advective-Reflective Conceptual Model for the Oscillatory Nature of the ENSO. *Sci.* **277**(5326): 663-666.
- Saha S, Nadiga S, Thiaw C, et al. 2006. The NCEP Climate Forecast System. *J. Clim.* **19**(15): 3483-3554.
- Sainivas G, Chowdary GS, Kosaka Y. 2017. Influence of the Pacific–Japan Pattern on Indian Summer Monsoon Rainfall. *J. Clim.* **31**: 3943-3958.
- Stockdale TN, Anderson DLT, Balmaseda MA, et al. 2011. ECMWF seasonal forecast system 3 and its prediction of sea surface temperature. *Clim. Dyn.* **37**(3-4): 455-471.
- Su JZ, Zhang RH, Rong XY et al. 2010. Causes of the El Niño and La Niña amplitude asymmetry in the equatorial eastern Pacific. *J. Clim.* **23**(3): 605-617.

- Suarez MJ. 1988. A delayed action oscillator for ENSO. *J. Atmos. Sci.* **45**(21): 3283-3287.
- Tangang FT, Hsieh WW, Tang B. 1997. Forecasting the equatorial Pacific sea surface temperatures by neural network models. *Clim. Dyn.* **13**: 135–147.
- Wang B, Wu R, Fu X. 2000. Pacific-East Asian Teleconnection: How Does ENSO Affect East Asian Climate? *J. Clim.* **13**(9): 1517-1536.
- Wang B, Li J, He Q. 2017. Variable and robust East Asian monsoon rainfall response to El Nino over the past 60 years (1957–2016). *Adv. Atmos. Sci.* **34**(10), 1235-1248,
- Wang C, and Picaut J. 2004. Understanding ENSO physics-A review, in Earth's Climate: The Ocean-Atmosphere Interaction, *Geophys. Monogr. Ser.* **147**: 21-48.
- Wang SY, L'Heureux M, Chia HH. 2012. ENSO prediction one year in advance using western North Pacific sea surface temperatures. *Geophys. Res. Lett.* **39**.
- Wyrtki K. 1975. El Niño—the dynamic response of equatorial Pacific Ocean to atmospheric forcing. *J. Phys. Oceanogr.* **5**: 572–583.
- Weisberg RH, Wang C. 1997. A Western Pacific Oscillator Paradigm for the El Niño–Southern Oscillation. *Geophys. Res. Lett.* **24**: 779–782.
- Xiang B, Wang B, Li T. 2013. A new paradigm for the predominance of standing Central Pacific Warming after the late 1990s. *Clim. Dyn.* **41**(2).
- Yu JY, Kim ST. 2011. Reversed Spatial Asymmetries between El Niño and La Niña and Their Linkage to Decadal ENSO Modulation in CMIP3 Models. *J. Clim.* **24**(20): 5423-5434.
- Zhu J, Kumar A, Huang B, et al. 2016. The role of off-equatorial surface temperature anomalies in the 2014 El Niño prediction. *Sci. Rep.* **6**(1): 19677.
- Zhu XT. 2018. Simulation of Sea Level Variations in The Tropical Pacific Using A Linear Multi-mode Model with Application to The Emergence of Central Pacific ENSO (Doctoral thesis/PhD), *Christian-Albrechts-Universität Kiel, Kiel, Germany*, 95 pp.
- Zhu ZW, Li T, Hsu PC, He JH. 2015. A spatial–temporal projection model for extended-range forecast in the tropics. *Clim. Dyn.* **45**: 1085–1098.
- Zhu ZW, Li T. 2016. A new paradigm for continental U.S. summer rainfall variability: Asia–North America teleconnection. *J. Clim.* **29**: 7313–7327.
- Zhu ZW, Li T. 2017. The statistical extended-range (10–30-day) forecast of summer rainfall anomalies over the entire China. *Clim. Dyn.* **48**(1): 209-224.
- Zhu ZW, Li T. 2018a. Amplified contiguous United States summer rainfall variability induced by East Asian monsoon interdecadal change. *Clim. Dyn.* **50**(9-10): 3523-3536.
- Zhu ZW, Li T. 2018b. Extended-range forecasting of Chinese summer surface air temperature and heat waves. *Clim. Dyn.* **50**(5-6): 2007-2021.

Table captions

Table 1. Definition of predictors in the STPM.

Table 2. RMSE as a function of lead time from one to six months.

Figure captions

Figure 1. Flowchart of the STPM, in which X , Y , U_k , V_k , u_k and v_k are the standardized predictor, standardized predictand, k th singular vectors of the predictor, k th singular vectors of the predictand, and corresponding time expansion coefficient of the predictor and predictand, respectively; i_1 (j_1) and i_2 (j_2) are the zonal (meridional) grids for the predictor and predictand fields; t represents the temporal grids; n_1 (n_2) denotes n_1 (n_2) months leading (lagging) to time t in the training period; the number of SVD modes is K ; m and M indicate the m th and total number of SVD modes exceeding the significance level of 99% during cross-validation; t_p is the independent forecast period; and Y_p is the initial forecasted predictand; the ratio between the standard deviation of the observed predictand fields and the standard deviation of the reconstructed predictand fields during 1950–2000 is applied as empirical values (*ratio*); and Y_p^* is the final forecasted predictand.

Figure 2. Evolution of MLTA regressed onto Niño3.4 index in JAS (top panel), SON (middle panel) and NDJ (bottom panel) during 1950–2000 based on SODAv2.2.4 data. The temporal evolution of MLTA is two-month averaged. For example, in the top panel, Oct.(–1) represents the average of Oct.(–1) and Nov.(–1) MLTA regressed onto JAS(0) Niño3.4 index. The dots denote anomalies exceeding the 0.05 significance level. The notation ‘(0)’ and ‘(–1)’ indicates the current and preceding year, respectively.

Figure 3. As in Fig. 2, but for the SSTA during 1950–2000 based on ERSST.v5 data. The green box (5°S–5°N, 160°E–80°W) denotes the critical domain selected for prediction.

Figure 4. As in Fig. 2 but is D20CA during 1950–2000 based on SODAv2.2.4 data. The green box is (5°S–5°N, 160°–100°W) denotes the critical domain selected for prediction.

Figure 5. Niño3.4 index (red solid line) predicted by MLTA and the observed Niño3.4 index (black dashed line) in JAS(0) to DJF(+1) from 2001 to 2016. The top central number is the RMSE between the predicted and observed Niño3.4 index. The MLTA datasets are from SODAv2.2.4 during 2001–2008 and GODAS during 2009–2016.

Figure 6. As in Fig. 5 but for the SSTA derived from ERSST.v5 data.

Figure 7. As in Fig. 5 but for D20CA. The D20CA datasets are from SODAv2.2.4 during 2001–2008 and GODAS during 2009–2016.

Figure 8. As in Fig. 5 but for AWI calculated based on NCEP/NCAR data.

Figure 9. Niño3.4 index in DJF predicted by MLTA (green line), SSTA (yellow line), D20CA (orange line) and AWI (purple line), along with the observed DJF Niño3.4 index (black line). The ensemble-mean and the persistent (Niño3.4 index in June) forecasts are denoted by the red and gray line, respectively. The RMSE is shown in the upper-right (upper left) of the panel for each predictor during independent-forecast period in 2001-2016 (hindcast period in 1950-2000).

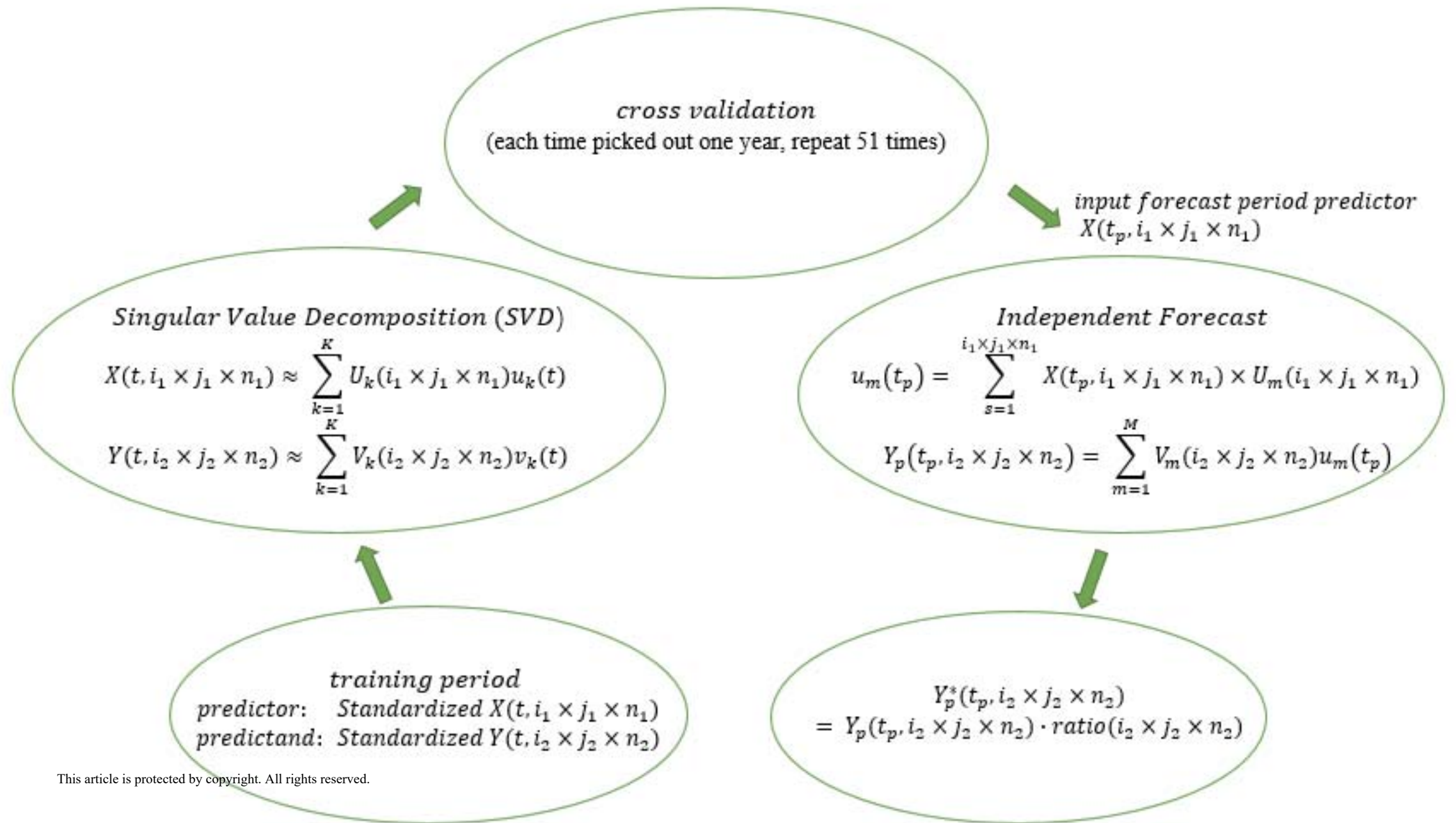
Figure 10. Scatterplot of observed and forecasted Niño3.4 index in DJF (x-axis is observation, y-axis is the prediction). The circles with a radius of 0.5°C and 1°C divide the events into three categories based on the forecasted Niño3.4 index: normal events (radius less than 0.5°C); weak ENSO events (radius more than 0.5°C and less than 1°C); and strong ENSO events (radius more than 1°C). The correlation coefficients between the observed and predicted Niño3.4 index in each category are shown in the bottom right of the figure. Red dots (blue triangles) represent ensemble STPMs forecasted (persistent forecasted) Niño3.4 index. The big red dots and the big blue triangles denote the averaged mean of the total STPM forecasted and persistent forecasted Niño3.4 index in positive and negative signs.

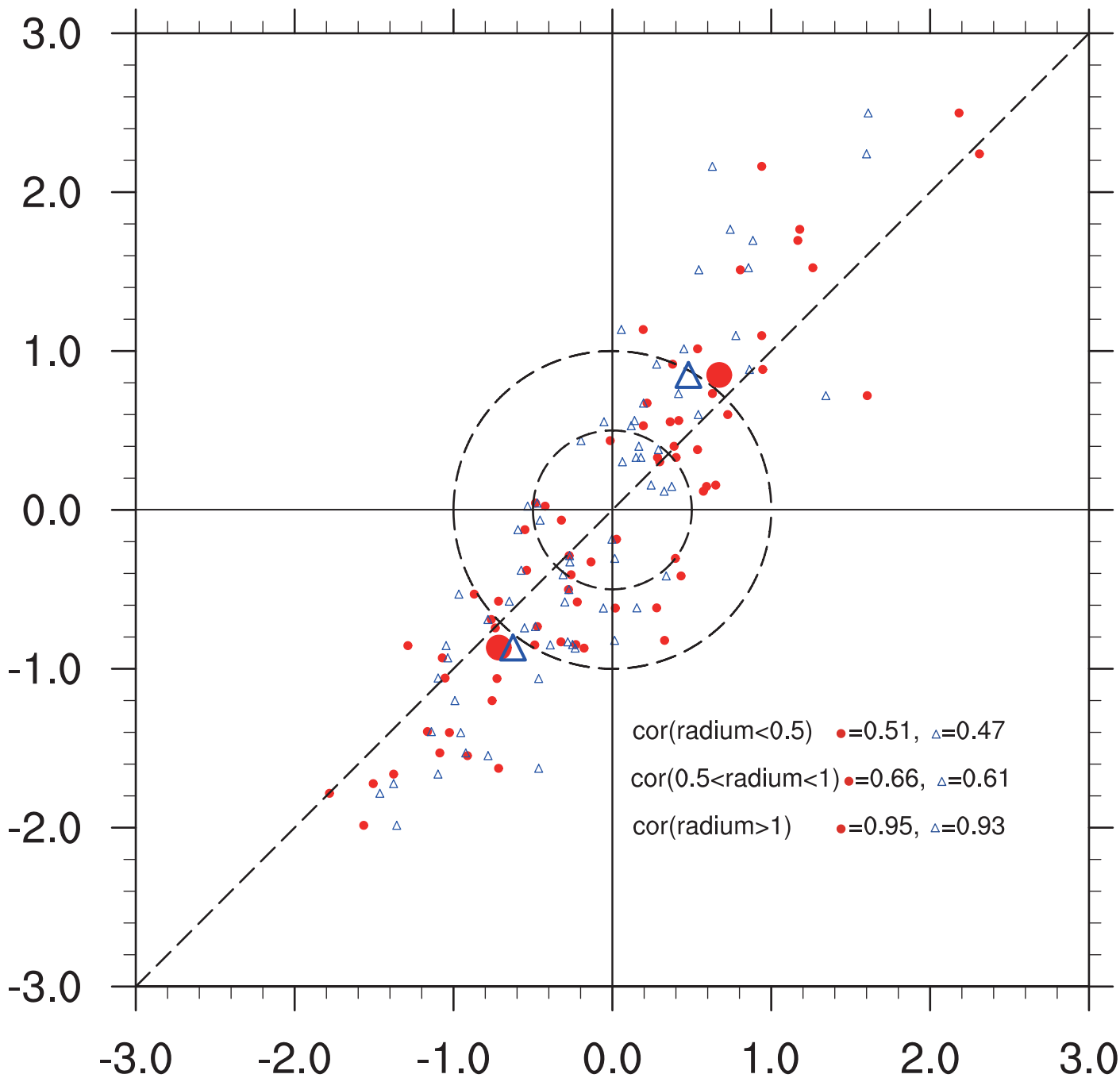
Table 1. Definition of predictors in the STPM.

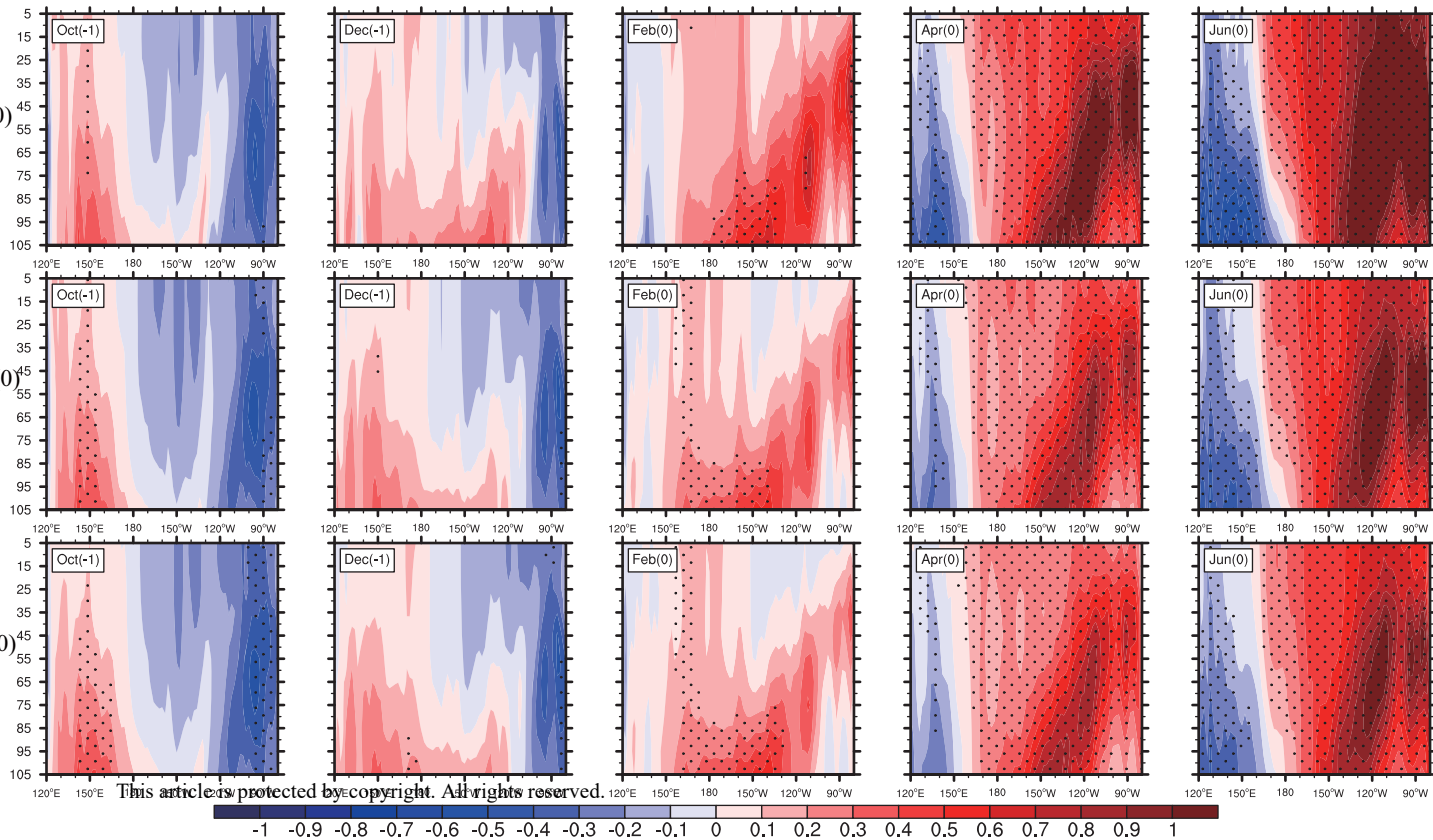
Predictor	Definition	Physical meaning
MLTA	Vertical pattern (5–105 m, 120°E–80°W) of the mixed-layer temperature anomaly averaged over 5°S–5°N	The maximum positive (negative) anomalous temperature center is in the subsurface, contributing to positive (negative) temperature advection through mean upwelling by thermocline feedback ($-\bar{w} \frac{\partial T'}{\partial z}$).
SSTA	Horizontal pattern of the SSTA over (5°S–5°N, 160°E–80°W)	SST persistence and SST evolution.
D20CA	Horizontal pattern of the thermocline depth (defined as the depth of the 20°C isotherm) anomaly over (5°S–5°N, 160°–100°W)	$u_g' = -\frac{g'}{\beta} \frac{\partial^2 h'}{\partial y^2}$, where h' is D20CA, which means a positive (negative) thermocline depth anomaly along the equator will lead to positive (negative) geostrophic currents. Eastward (westward) zonal current anomalies contribute to warm (cold) advection by zonal advection feedback ($-u' \frac{\partial T'}{\partial x}$).
AWI	Accumulated WWE index (which is obtained through integrating the monthly WWE-index). The WWE-index on a given day is obtained by integrating the WWE-Taux' over the WWE-region (5°S–5°N, 120°E–180). The WWE-Taux' is obtained by extracting the 90-day high-frequency (HF) component of zonal wind stress (Taux), then subtracting the annual cycle, and calculating a climatological standard deviation (Std) field. Next, when the HF-Taux' is greater than one HF-Std, the exceeding part is referred to as WWE-Taux' (i.e., WWE-Taux' = HF-Taux' minus HF-Std).	The pulses of WWE-Taux' match well with the flaring up of h' over the CEP. WWE forcing may play an essential role in the sudden emergence and continuous intensification of positive h' over the CEP, thus contributing to ENSO's formation (Chen et al. 2017).

Table 2. RMSE as a function of lead time from one to six months.

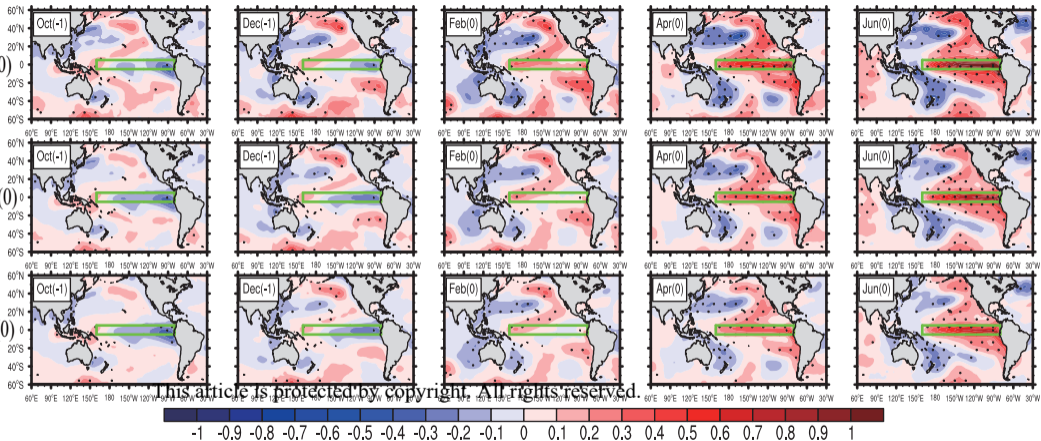
Lead months	1	2	3	4	5	6
RMSE	0.20	0.28	0.38	0.46	0.52	0.52

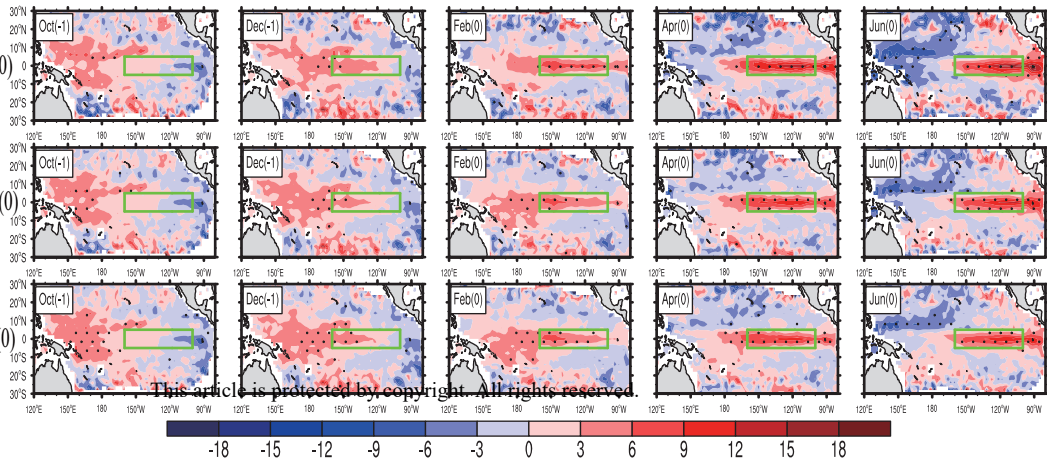






This article is protected by copyright. All rights reserved.





This article is protected by copyright. All rights reserved.

